



Supporting Online Material for

Dislocation Avalanches, Strain Bursts, and the Problem of Plastic Forming at the Micrometer Scale

Ferenc F. Csikor, Christian Motz, Daniel Weygand,
Michael Zaiser, Stefano Zapperi*

*To whom correspondence should be addressed. E-mail: stefano.zapperi@roma1.infn.it

Published 12 October 2007, *Science* **318**, 251 (2007)
DOI: 10.1126/science.1143719

This PDF file includes:

SOM Text
Figs. S1 to S4
References

Supporting online material

Ferenc F. Csikor^{1,2}, Christian Motz³, Daniel Weygand³,
Michael Zaiser², Stefano Zapperi^{4,5}

¹ Department of Materials Physics, Eötvös University,
PO Box 32, H-1518 Budapest, Hungary

² Center for Materials Science and Engineering, University of Edinburgh,
King's Buildings, Sanderson Building, Edinburgh EH93JL, UK

³ Universität Karlsruhe, Institut für die Zuverlässigkeit
von Bauteilen und Systemen, Kaiserstr. 12, 76131 Karlsruhe, Germany

⁴ CNR-INFM, SMC, Dipartimento di Fisica, Sapienza — Università di Roma,
P.le A. Moro 2, 00185 Roma, Italy

⁵ ISI Foundation, Viale S. Severo 65, 10133 Torino, Italy

Discrete dislocation dynamics

In three dimensional discrete dislocation dynamics (3DDD) simulations, plastic flow of single crystals is modelled by explicitly tracing the motion of dislocations, the carriers of plasticity. Dislocations are one dimensional line defects, whose elastic properties are well described within the framework of linear elasticity (*S1*). In the literature, various discrete dislocation dynamics models can be found which differ in the way dislocations are broken into discrete segments and how boundary conditions for finite specimens are handled (*S2-S5*). The current investigation is performed using a 3DDD simulation code which is optimized for small scale plasticity of finite, cuboid-shaped fcc single crystals. Details can be found in (*S6-S7*). In the model dislocations are represented as series of straight segments. Based on the superposition approach of van der Giessen (*S8*), image correction fields are used to turn the analytically-known infinite-volume dislocation interaction fields

into their finite-volume counterparts. This approach allows us to apply arbitrary boundary conditions to the sample. In particular, both displacement and traction boundary conditions can be imposed.

The dislocation motion is assumed to be conservative (i.e. only glide motion is considered and climb is excluded) and fcc crystallography is used. A second-order equation of motion for the dislocations is solved which includes both viscous damping and dislocation inertia. Dislocation segments may form junctions upon contact, and dislocations of opposite Burgers vectors may annihilate. Depending on temperature and stacking-fault energy, dislocations may change their glide plane by cross-slip events. We can test directly whether this mechanism, which allows the dislocations for instance to overcome a particularly strong obstacle, is relevant by turning it on and off and then comparing the results. For the presented simulations we chose elastic constants, dislocation mobility, dislocation mass and cross slip parameters to capture the behavior of Al at room temperature.

The standard volume V used in our simulations was $(0.5 \mu\text{m})^3$, and the initial dislocation density ρ was $9 \times 10^{13} \text{ m}^{-2}$. Dislocations were initially distributed in the form of randomly placed sources (segments with both ends pinned, located and oriented randomly under the constraint that their ends do not pierce the specimen surface); for a cube of 0.5 micron edge length, 4 source segments of average length 0.2 micron were placed on each of the 12 possible slip systems. The sources had uniform length, however, an exponential source length distribution resulted in similar burst statistics if initial transients were excluded from the analysis. In the simplest situation, we considered single slip deformation where compression occurred along the $[269]$ crystal axis. This is directly relevant for the compression experiments on micropillars. In other simulations, we considered multiple slip conditions with the compression axis along $[100]$ and $[110]$ lattice directions.

An important issue concerns the driving rate (stress or strain rate) imposed in the

simulations. A low imposed driving rate greatly increases the computational cost, whereas a too high driving rate may change the behavior of the dislocation system as dislocation motion is governed by the external driving force rather than their mutual interactions. A pragmatic criterion for finding the 'right' driving rate is to require that the statistical properties of the dynamics do not appreciably change if the driving rate is decreased. For our 'standard' simulation described above, this pragmatic criterion led to an imposed strain rate of $5 \times 10^3 \text{ s}^{-1}$ in a displacement-controlled simulation. For stress controlled simulations, the driving stress rate was determined by multiplying this rate with the characteristic slope Θ of the stress-strain curve in the plastic regime. Imposing larger driving rates resulted in overlapping bursts, whereas smaller driving rate left the strain burst statistics unchanged. To avoid burst overlap, the driving rates for larger systems were then reduced in inverse proportion with the system volume when larger systems were simulated. This constraint gave a very strong practical limit to the system sizes that could be computed.

Our simulations differ from 'standard' dislocation dynamics simulations in the sense that the simulated system sizes are smaller than in most simulations reported in the literature, whereas the dislocation densities and strain rates are higher. In this context it is useful to recall a fundamental scaling property of dislocation systems: Let us assume that dislocation motion is over-damped such that the dislocation glide velocity is proportional to the resolved shear stress (this is approximately true for our simulations where the maximum dislocation velocities are still a small fraction of the sound velocity), and that dislocations only interact with each other (no other obstacles, no significant lattice friction). Let us further assume that, under these conditions, simulation of a system of size L , dislocation density ρ , and imposed strain rate $\dot{\epsilon}$, yields a flow-stress curve $\sigma(\epsilon)$. One can then re-scale this simulation to yield a simulation with size aL , density ρ/a^2 , and

strain rate $(1/a)\dot{\epsilon}$. The corresponding flow stress curve is σ/a at strain ϵ/a . In this sense, our 'typical' simulation described above is, with $a = 10$, equivalent to the simulation of a system of size $5\mu\text{m}$, dislocation density 10^{12} m^{-2} , and imposed strain rate $\dot{\epsilon} = 5 \times 10^2 \text{ s}^{-1}$. Note that the scaling relation for the maximum avalanche strain, Eq. (2), is consistent with this fundamental scaling property.

To determine the hardening slope Θ , average stress-strain curves were determined by averaging over multiple (typically more than 10) statistically equivalent simulations that differed only in the initial location of the dislocation sources. These graphs could in general be clearly divided into initial linear elastic and later linear hardening parts with slope Θ . Strain burst statistics were determined over the linear hardening parts only, discarding any bursts occurring within the initial transient. Two examples of average stress-strain curves are shown in Figure S3. The upper curve in that figure corresponds to a 'standard' cube specimen deformed in tension/compression along the $[100]$ lattice axis. The large value $\Theta = E/10$ observed in this case is caused by dislocations piling up against the rigid top and bottom surfaces of the specimen, leading to kinematic hardening. The lower curve corresponds to an elongated $[100]$ specimen (aspect ratio 2:1:1). In this case, kinematic hardening is almost absent as moving dislocations can leave the specimen through its free side faces. The hardening slope $\Theta \approx E/50$ in this case is in line with the initial hardening of $[100]$ oriented bulk single crystals.

In addition to single crystals we performed some simulations on bi-crystals and multi-crystals in order to assess the influence of grain boundaries (GB) on the strain burst dynamics. In these simulations, GB were treated as rigid boundaries between crystal-lites of different orientation, allowing neither dislocation transmission nor the emission of dislocations from the boundary. Bi-crystals were constructed by assembling two 'standard' cube crystals of different orientation; initial conditions within each of the cubes

were similar to those in the single crystal simulations. Multi-crystals were assembled as 3×3 arrays of elementary cubes of random orientation; in this case the initial dislocation density was reduced by a factor of 4 to keep the computational cost affordable. Avalanche strain distributions in these simulations followed Eq. (1) with the same exponent $\tau \simeq 1.5$ as in single crystals but with a smaller cutoff; this reduction in avalanche strains could be interpreted in terms of dislocation avalanches being essentially confined to single crystallites (see Figure S4). We note that by allowing only elastic interactions between different crystallites we probably over-estimate the impact of grain boundaries on the avalanche dynamics – real GB’s may transmit or emit dislocations, thus allowing dislocation avalanches to extend across different grains.

The avalanche cutoff

The size-dependent cutoff s_0 in the avalanche strain distribution can be obtained by generalizing a simple mean-field scaling relation discussed in Ref. (S9). To this end, we envisage an avalanche as a branching process (S10) consisting of discrete ‘elementary events’ producing a strain s_{el} within some volume V_{el} . This event produces in the same volume a back stress of order Es_{el} , and stress equilibrium requires that this is balanced by an average forward stress Es_{el}/N shed on all N other volume elements of the system. In reality, stress re-distribution is inhomogeneous and anisotropic, but the basic scaling properties are not affected by these details. This forward stress may trigger additional events with a probability p that depends on the externally applied stress σ :

$$p(\sigma) = \chi(\sigma)Es_{\text{el}}/N . \quad (\text{S1})$$

Here χ is their stress susceptibility, i.e. the probability that a susceptible volume element is triggered by a unit stress increase. For a short-range model on a lattice the number of susceptible elements N_{susc} is equal to the lattice coordination number, while

for an infinite-range mean-field model where all elements are independent and equivalent, $N_{\text{susc}} = N$. In the present case, where the interactions are long-ranged and anisotropic, N_{susc} is imposed by the slip geometry.

For a branching process, the average number of events

$$\langle n \rangle = \frac{1}{1 - pN_{\text{susc}}} \quad (\text{S2})$$

diverges at some critical stress σ_c where $\chi(\sigma_c) = N/(N_{\text{susc}}Es_{\text{el}})$. We expand the susceptibility around this stress level, $\chi = \chi(\sigma_c) - \chi'(\sigma_c - \sigma)$, and note that the characteristic stress scale of the problem is set by $(N_{\text{susc}}/N)Es_{\text{el}}$, implying that $\chi' \propto [N/(N_{\text{susc}}Es_{\text{el}})]^2$. This yields

$$\langle n \rangle = \frac{AEs_{\text{el}}N_{\text{susc}}}{N(\sigma_c - \sigma)}, \quad (\text{S3})$$

where A is a numerical constant. For $\sigma \rightarrow \sigma_c$, the system would reach its critical point where the average avalanche size diverges. In our situation, however, the propagation of an avalanche reduces the effective stress by an amount that is proportional to the avalanche strain (note that, in a mean-field picture, the local stress relaxation due to hardening and the global stress relaxation due to the machine are equivalent). Hence, the system remains, on average, by an amount $\sigma_c - \sigma \approx (\Theta + \Gamma)\langle n \rangle s_{\text{el}}/N$ below the critical point. Combining these relations, we find that

$$\langle n \rangle^2 = \frac{AEN_{\text{susc}}}{(\Theta + \Gamma)}. \quad (\text{S4})$$

Next, to obtain the avalanche cutoff, we resort again to the branching process picture (S10). The avalanche distribution can be computed exactly for a branching process and is given by $P(n) = n^{-3/2}f(n/n_0)$, where $f(x)$ is a cutoff function (S10). The branching process picture turns out to be quantitatively correct for dislocation avalanches because long-range interactions between the dislocations turn this into a mean-field problem (S9).

It is then straightforward to show that the number of elementary events in the largest avalanches is related to the average by $n_0 \approx \langle n \rangle^2$. The corresponding strain is $s_0 = s_{el} n_0 / N$ where we can set $s_{el} = 1$. If the largest avalanches are fractal objects of dimension d_f and extension ξ which may encompass a fraction $N_{av} / N = \xi^{d_f} b^{3-d_f} / V$ of the crystal volume V . Combining all these relations, we find that the cutoff strain scales as

$$s_0 \propto \frac{E}{\Theta + \Gamma} \left(\frac{\xi^{d_f} b^{(3-d_f)}}{V} \right). \quad (\text{S5})$$

We illustrate this relation for a few simple cases. For a pure mean-field model implemented on a cube of edge length L , $N_{av} = N$, so $\xi = L$, $d_f = 3$, and $s_0 \approx \frac{E}{\Theta + \Gamma}$. In case of our dislocation dynamics simulations, strong correlations between the elementary deformation events are caused by the fact that these are due to the motion of dislocation lines along prescribed planes. For the largest avalanches in single crystals, most of the strain is concentrated on a few slip planes which span the entire cross-section of the sample, hence $\xi = L$ and $d_f \simeq 2$. For cubic single crystals of edge length L , $\xi = L$ and $V = L^3$, such that we recover Eq. (2). For elongated single crystals, ξ is the transverse dimension of the specimen, and $V = L\xi^2$ where L is now the specimen length, again recovering Eq. (2). For polycrystals, our simulations indicate that ξ is the grain size. Accordingly, the avalanche strain is reduced by a factor $(\xi/L)^2$ with respect to the single crystal case. For the case of the bi-crystal simulations, we have that the transverse dimension is L and the total crystal volume is $2L^3$. Hence the avalanche strain cutoff s_0 should be exactly half of the one observed in a single crystal of volume L^3 . This is demonstrated in Figure S4.

The dissipated energy e during an avalanche is simply proportional to the strain s : $e = \sigma s V$. Hence, the cutoff of the avalanche energy distribution increases as $e_0 \propto \xi^2$. If we assume that the acoustic energy is proportional to the dissipated energy, we understand why acoustic emission avalanches are observed in macroscopic single crystals, while strain

avalanches are not. Notice that in several instances, papers in the literature report the distribution of acoustic emission amplitudes $P(a)$. Amplitudes and energies are related by $e = a^2$. Hence, we would expect the amplitude distribution cutoff to scale as $a_0 \propto \xi$. In addition, it is also possible to derive a scaling relation for the exponent τ_a of the amplitude distribution. Conservation of probability imposes that $P(a)da = P(e)de$. Using the relation between e and a we then obtain $\tau_a = 2\tau - 1$. Hence, $\tau = 3/2$ corresponds to $\tau_a = 2$, in agreement with experiments (S11).

Stochastic continuum simulation of bending

We exploit the universality of the strain burst characteristics to implement a stochastic continuum simulation of the bending of a thin rod with square cross-section. We assume that a torque is applied symmetrically to both ends of the rod such that the bending moment M_b is constant along its length.

We start out from a simple rate-dependent constitutive model which gives the local plastic strain rate $\dot{\epsilon}_b$ as

$$\dot{\epsilon}_b = C \left(\frac{M_b/t^3}{\Theta \epsilon_b} \right)^m \quad (\text{S6})$$

where C is a constant, t is the thickness of the rod, Θ is the hardening rate of the material (which we assume for simplicity to be constant), and m is a rate exponent.

We now generalize this constitutive model in a stochastic sense to account for the fact that deformation occurs as an intermittent sequence of discrete strain bursts. To this end, we break the rod into segments of length t . Deformation of each segment is assumed to occur as a sequence of strain bursts which produce strain increments (again understood as surface strains) $\Delta\epsilon_i = s_i$ that are drawn independently from the universal distribution given by Eq. (1) with a cutoff that obeys Eq. (2), where the characteristic dimension L

is identified with t . In natural generalization of Eq. (S6), the burst rate is assumed as

$$r = \frac{C}{\langle s_i \rangle} \left(\frac{M_b/t^3}{\Theta \sum_i s_i} \right)^m, \quad (\text{S9})$$

and the average strain rate is just $r\langle s_i \rangle$. We have implemented this scheme for a rod with an aspect ratio of 1:50, which we discretize into 50 segments which are assumed to behave independently. Deformation is most homogeneous in the limit $m \rightarrow \infty$, when the model reduces to an extremal dynamics: In this case, the event rate is strongly enhanced in the segment with the smallest local deformation, leading to a deformation process which is the 'most homogeneous' possible that is consistent with the burst statistics, Eq. (1). M_b was increased until the total bending angle exceeded 2π . Doing so for different rod thicknesses (i.e. different cut-off values s_0) and with a high rate exponent $m = 10$ typical of fcc metals leads to the shapes shown in Fig 4.

Supplementary Figures and Legends

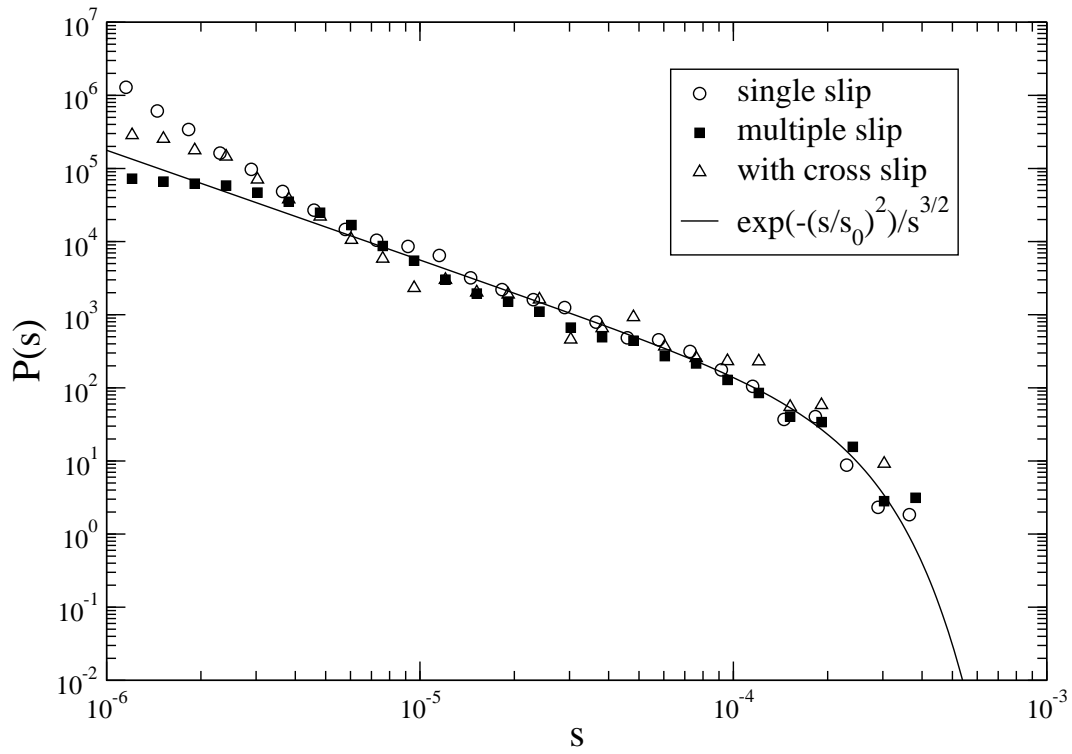


Figure S1: The distribution of avalanche strains for different slip geometries. The shape of the distributions obtained under displacement control is insensitive to the presence of single or multiple slip systems and to the activation of cross slip, indicating universality with respect to slip geometry.

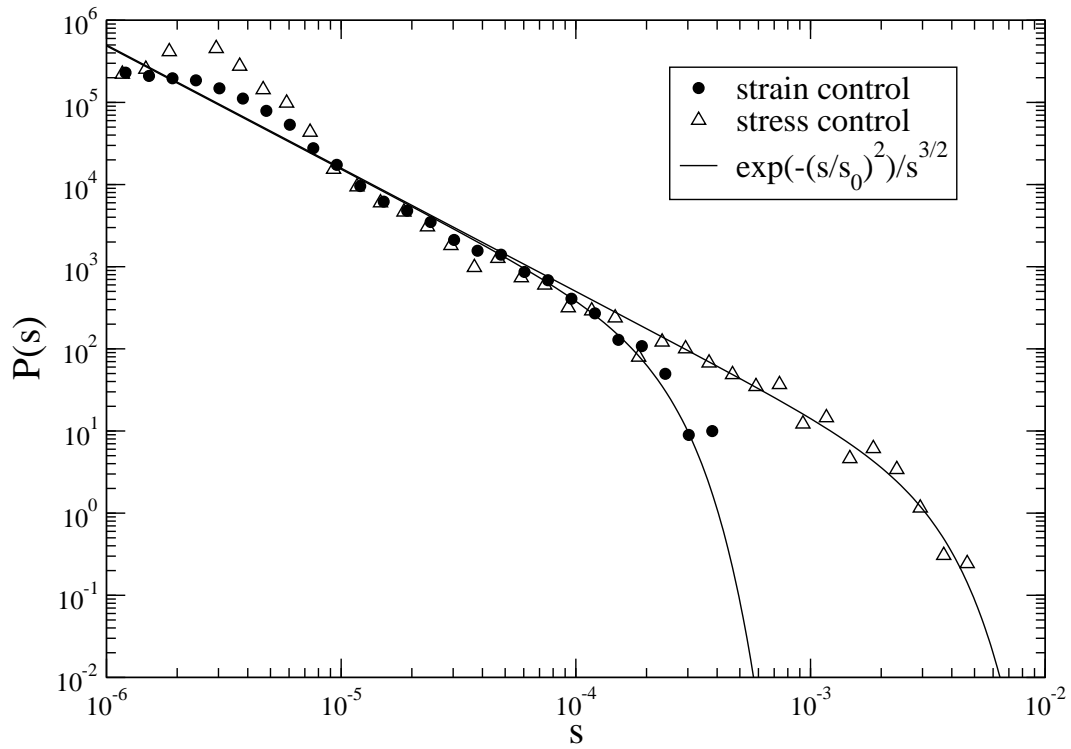


Figure S2: The distribution of avalanche strains under different loading conditions. The cutoff of the distributions obtained under load-controlled deformation is larger

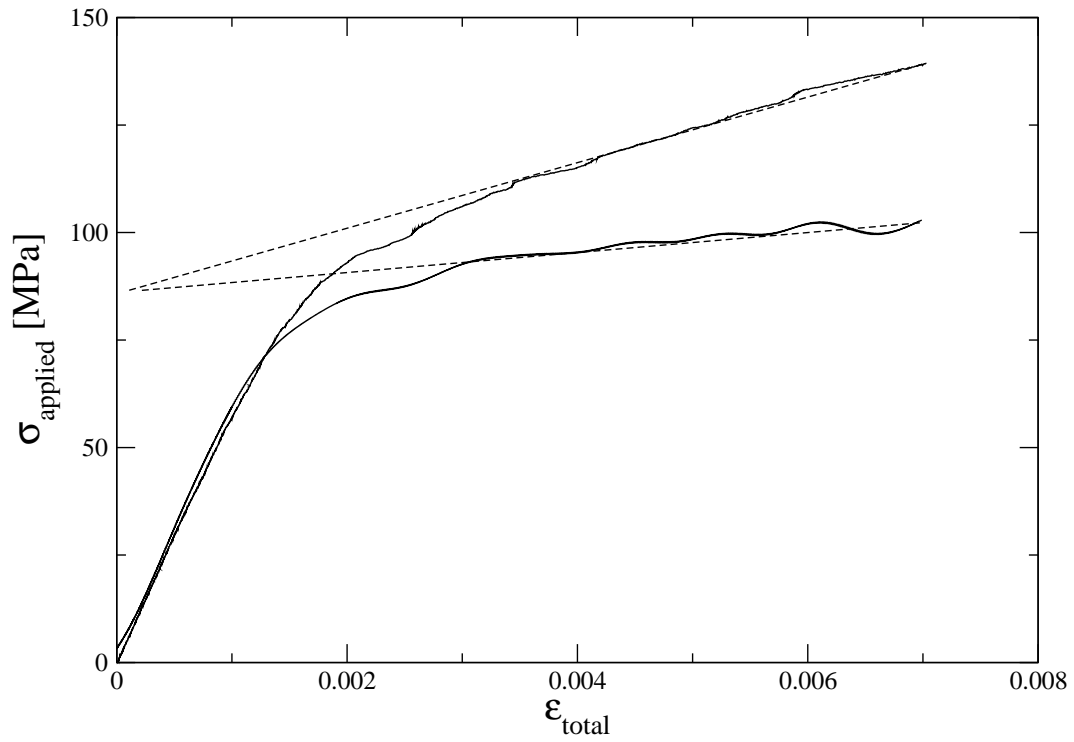


Figure S3: Average stress-strain curves for [100] oriented specimens. Top curve: cube specimens. Bottom curve: (2:1:1) parallelepipeds. Dashed lines: linear hardening fits to determine strain hardening coefficients Θ .

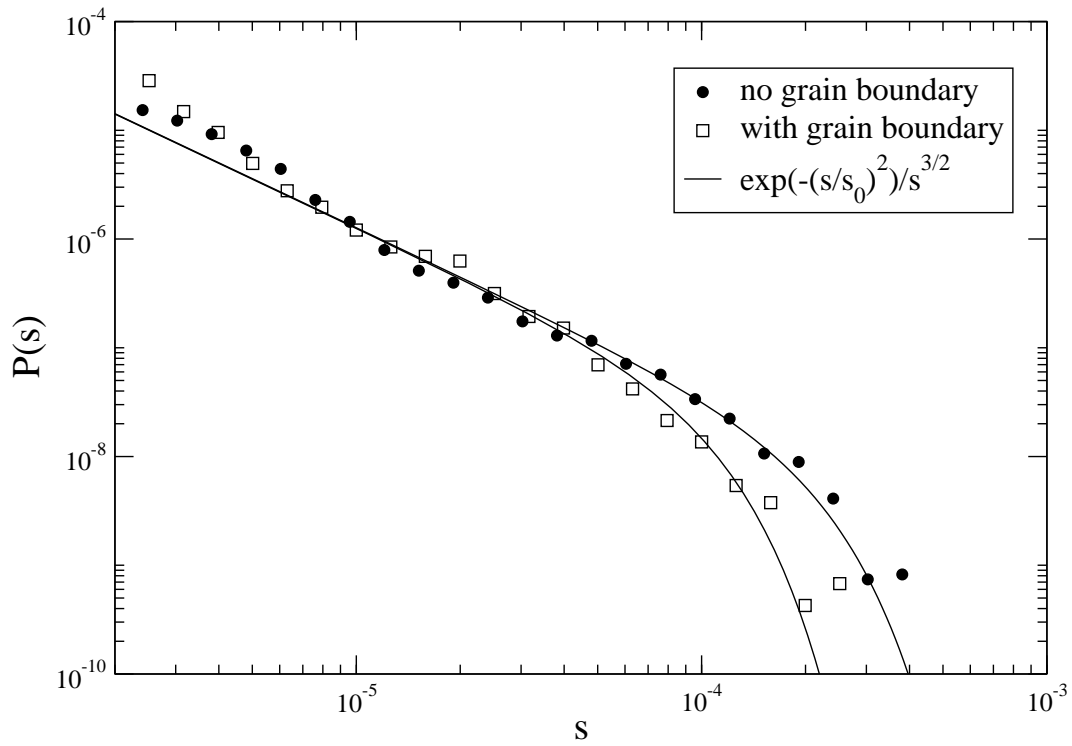


Figure S4: The distribution of avalanche strains in presence of a grain boundary as compared with the single crystal. The shape of the distribution is the same but the cutoff value in presence of a grain boundary is reduced by a factor 2.

Supplementary references

- S1* J. P. Hirth, J. Lothe, *Theory of Dislocations* (Krieger Publishing Company, 1992).
- S2* L. P. Kubin, *et al.* in *Nonlinear Phenomena in Materials Science* vol II ed. Martin, G. Kubin, L. P., 455 (Sci-Tech, Vaduz, 1992).
- S3* H. M. Zbib, M. Rhee, J. P. Hirth, *Int. J. Mech. Sci.* **40**, 113 (1998).
- S4* K. W. Schwarz, *J. Appl. Phys.* **85**, 108 (1999).
- S5* N. M. Ghoniem, L. Z. Sun, *Phys. Rev. B* **60**, 128 (1999).
- S6* D. Weygand, L. H. Friedman, E. van der Giessen, A. Needleman, *Modelling Simul. Mater. Sci. Eng.* **10**, 437 (2002).
- S7* D. Weygand, P. Gumbsch, *Mat. Sci. Eng A* **400–401**, 158 (2005).
- S8* E. van der Giessen, A. Needleman, *Modelling Simul. Mater. Sci. Eng.* **3**, 689 (1995).
- S9* M. Zaiser, P. Moretti, *J. Stat. Mech.* P08004 (2005).
- S10* S. Zapperi, K. B. Lauritsen, H. E. Stanley, *Phys. Rev. Lett.* **75**, 4071 (1995).
- S11* T. Richeton, J. Weiss, F. Louchet, *Nature Mat.* **4**, 465 (2005).